Radiation Physics and Chemistry 167 (2020) 108354

Contents lists available at ScienceDirect

Radiation Physics and Chemistry

journal homepage: www.elsevier.com/locate/radphyschem

Soft X-rays spectroscopy with a commercial CMOS image sensor at room temperature☆

Miguel Sofo Haro[a,c,*], Fabricio Alcalde Bessia[b,c], Martín Pérez[a,c], Juan Jerónimo Blostein[b,c], Darío Federico Balmaceda[c], Mariano Gomez Berisso[b,c], José Lipovetzky[a,b,c]

[a] Comisión Nacional de Energía Atómica (CNEA), Centro Atómico Bariloche (CAB), Argentina
[b] Consejo Nacional de Investigaciones Científicas y Técnicas (CONICET), Argentina
[c] Instituto Balseiro, Universidad Nacional de Cuyo, Argentina

ARTICLE INFO

Keywords:
X-rays spectroscopy
CMOS image sensors (CIS)
CMOS active pixel sensor (APS)
Front-side illuminated
Charge transport
Single-photon
Incomplete charge collection (ICC)
Charge collection efficiency (CCE)

ABSTRACT

Besides their application in point and shoot cameras, webcams, and cell phones, it has been shown that CMOS image sensors (CIS) can be used for dosimetry, X-ray and neutron imaging applications. In this work we will discuss the application of an ON Semiconductor MT9M001 CIS, in low energy X-ray spectroscopy. The device is a monochromatic front-side illuminated sensor, very popular in consumer electronics. In this work we introduce the configuration selected for the mentioned sensor, the image processing techniques and event selection criteria, implemented in order to measure the X-ray energy in the range from 1 to 10 keV. Several fluorescence lines of different samples have been resolved, and for first time the line resolution have been measured and analyzed. We achieved a FWHM of 232 eV at 6.4 keV, and we concluded that incomplete charge collection (ICC) of the charge produced by the X-ray contributes to the resolution, being this effect more important at higher X-ray energies. The results analyzed in this work indicate that the mentioned CIS are specially suitable for X-ray applications in which energy and spatial resolutions are simultaneously required.

1. Introduction

Since their discovery in 1895 by Roentgen, X-rays have found a countless number of everyday applications in medicine, industry, and have been a powerful tool in material science and biology. Common technologies for their detection and energy measurement, are silicon drift detectors (SDD) and ad hoc detectors. In the field of big area X-ray radiography, due to their low cost compared to thousand of dollars flat panels, radiographic films still been the preferred option.

Nowadays CMOS image sensors (CIS) can be found in several consumer electronics products, like picture cameras and cell phones. They are mass-produced, have a low cost, and thanks to the integration in the same chip of the analog and digital reading electronics, can be easily integrated in embedded systems. In the last two decades, they have been used as charged particles and gamma photons detectors. For example in high resolution X-ray transmission imaging of small objects (Lane, 2012) (Hoidn and Seidler, 2015) (Castoldi et al., 2015) (Alcalde Bessia et al., 2018). Also, previous works have demonstrated the potential of these sensors for X-ray spectroscopy without analyzing the resolution capabilities of this devices (Lane, 2012) (Hoidn and Seidler, 2015) (Holden et al., 2018) (Nachtrab et al., 2009), which is the main objective of this work.

In Section 2 we present a brief overview of CIS physics, from the interaction of the X-rays with the silicon to the collection of charge in the pixels, which is necessary to interpret the experimental results introduced in this work. In Section 3 we will describe the employed sensor and the image processing technique followed to detect the X-ray lines emitted from the fluorescence of different materials. The response of the CIS at different X-ray energies, as well as the experimentally obtained energy resolution ere shown in Section 4. Finally, in Section 5, the read-out noise, energy resolution, dynamic range and efficiency of the detector will be analyzed.

2. X-ray spectroscopy with CIS

The most probable interaction mechanism of soft X-rays with silicon is the photoelectric effect, in which one atomic electron of the silicon absorbs the total energy of the incoming photon. The K-shell electrons, because of their proximity to the Silicon nucleus, have the highest probability of interacting with the photons (Grupen and Shwartz,

☆ Fully documented templates are available in the elsarticle package on CTAN.

* Corresponding author. Comisión Nacional de Energía Atómica (CNEA), Centro Atómico Bariloche (CAB), Argentina.
E-mail address: miguelsofoharo@gmail.com (M.S. Haro).

https://doi.org/10.1016/j.radphyschem.2019.108354
Received 15 December 2018; Received in revised form 30 May 2019; Accepted 4 June 2019
Available online 13 June 2019
0969-806X/

2008). When this interaction occurs, the K-shell electron is ejected from the Si atom with a kinetic energy $E_x - E_b$, where E_x is the energy of the X-ray and E_b is the binding energy for K-shell electrons. The electron produced, called photo-electron, is emitted in a wide angular range, being the most probable emission normal to that of the incoming the photon (Watson, 1928). This ejected electron produces an ionization trail of electron-hole pairs (e-h) through inelastic collisions with orbital electrons of the other silicon atoms. The K-shell vacancy could be filled by two mechanisms (Janesick, 2001). The mechanism with higher probability is the Auger process, in where the electrons from outer shells drop to inner ones as a free electron is ejected from the atom, thus producing a subsequent ionization (Janesick, 2001). The second, is the drop of an outer-shell electron to the K-shell generating a characteristic photon of ~ 1.78 keV for Silicon. This photon can escape from the detector or interact in the same or other pixel generating ~ 481 e-h pairs, producing a double event. All the released e-h pairs by the photo-electron and the Auger effect, on average will be distributed in a charge cloud with a Gaussian profile. The deviation σ_l of the profile is given by $0.257R_{e^-}$ (Yousef, 2011), where R_{e^-} is the range of the photo-electron that can be obtained from equation (1) (E_{e^-} in keV) (Yousef, 2011). As an example, an electron of 10 keV will produce its ionization in a cloud of radius ~0.25 μm (Williams, 2001) (Ashley et al., 1976) (Moody et al., 2017).

$$R_{e^-}(\mu m) = 0.0171E_{e^-}^{1.75} \quad (1)$$

The ionization produced by the photo-electron is a random process, therefore a finite and random fraction of the X-ray energy is transferred to the silicon in non-e-h processes (e.g, thermal excitation) (Janesick, 2001). The average number and variance are given by E_x/ω and FE_x/ω respectively (Janesick, 2001, F), where ω is the mean energy required to liberate one e-h pair. In silicon, at room temperatures (300 K), ω is equal to 3.62 eV (Groom et al., 2004, O). The constant F is called Fano Factor and its value is approximately ~ 0.115 (Janesick, 2001, F).

Standard CIS are fabricated over a heavily doped p-type thick substrate (p^{++}_{sub}, >~300 μm thick). Over it, a light-doped silicon epitaxial layer is grown (p^{-}_{epi}). Within the epitaxial layer n-type well structures are implanted (n^{+}_{well}), to form the n^{+}_{well}/p^{-}_{epi} diode junctions (~ 1 μm thick) that are the charge collection element of each CIS pixel (Meroli et al., 2011) (Meroli et al., 2012) (Esposito et al., 2017). Fig. 1 shows a schema of the transversal section of a CIS pixel.

The amount of collected charge will change depending in which region of the CIS it was generated. This effect has been previously observed and measured using high energy protons and electrons (Meroli et al., 2011) (Meroli et al., 2012), and simulated in (Esposito et al., 2017).

If the charge is generated inside the depleted region of the collection diode, all the charge will be collected. In field-free regions, like the epitaxial layer, the charge is transported to the collection diodes through a thermal diffusion process. Therefore it can be spread over neighboring pixels. The barrier introduced by the junction between the epitaxial layer and the substrate limits the charge diffusion towards the substrate (Esposito et al., 2017). In the previous region all the charge is collected, and therefore charge collection efficiency (CCE) is maximum. If the charge is generated in the substrate, it is also transported to the collection diodes through diffusion. Due to the high doping of this region and the distance to the collection diodes, the recombination losses are higher (Schroder, 1997), incurring in what is called in the bibliography as incomplete charge collection (ICC) loses. In this last case, the CCE falls exponentially. For example, for a CIS MT9V011, the CCE goes below 80% beyond 2 μm of the epitaxial layer (Meroli et al., 2012).

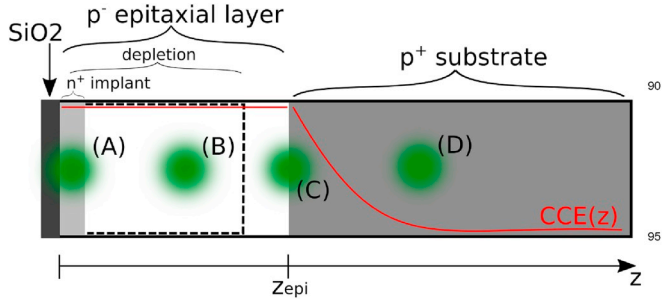

Fig. 1. Transversal section of a CIS pixel. The green clouds represents the charge produced by an X-ray interacting at different regions of the pixel. The curve in red, is the charge collection efficiency (CCE). In the epitaxial layer the CCE is maximum, and in the substrate, it falls exponentially. (For interpretation of the references to color in this figure legend, the reader is referred to the Web version of this article.)

Depending in which region of the CIS the X-ray interacts, will be the amount of collected charge. The charge cloud produced by an X-ray could be, in the epitaxial layer near the silicon oxide (case (A) of Fig. 1), totally in the epitaxial layer (case (B)), in the substrate (case (D)) or in an intermediate case, in where it is partially in the epitaxial layer and in the substrate (case (C)). In the case (A), part of the generated charge will be trapped in the silicon oxide, this effect have been previously characterized in CCDs (Prigozhin et al., 2000). In the cases (C) and (D), only a fraction of the charge will be collected, and the remaining fraction will be lost by recombination. For a certain X-ray energy, the final energy spectrum will be composed of events that had interacted in these four regions. If the X-rays have low energy, they will interact in the first few microns of the CIS in where the CCE is higher, and the spectrum will be composed mostly by events without ICC. For higher energy X-rays, they will interact more deep in the CIS, reaching the substrate and also producing a bigger charge cloud, and therefore events with ICC will be collected widening the peak shape. The final peak shape, will depends on the amount of X-rays that interacted in each region of the CIS.

3. Experimental method

An MT9M001 CIS manufactured by On Semiconductors was chosen for this work (ONSemi). It is a front-illuminated monochrome image sensor with 1280 × 1024 pixels of 5.2 × 5.2 μm^2 each one, covering a total area of 6.66 × 5.32mm^2. A previous work in our group estimated the epitaxial layer thickness in ~ 2μm (Bessia et al., 2018), together with its pixel size, a good spectral resolution is expected. In this work, the pixel voltage was read using with the internal 10-bit analog to digital converter (ADC). A previous demonstration of the X-ray spectroscopy capabilities of this sensor can be found in (Hoidn and Seidler, 2015). A custom printed circuit board was designed to operate the sensor and provide extra passive components, like power supply filtering and pull-up resistors. The custom board is connected to a board developed by the company Arducam (Arducam). It is an open hardware and software FPGA-based board that does the read-out of the CIS and transfers the data to a computer by an USB interface. A image of the whole system is shown in Fig. 2. To avoid X-ray attenuation, the protective glass that covers the CIS was removed, and to shield it against

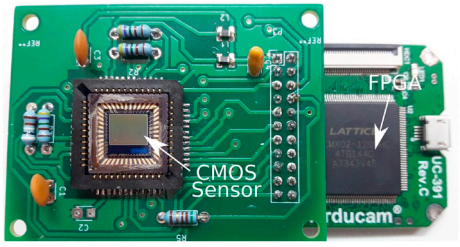

Fig. 2. Picture of the detector electronics. The CIS is installed in a custom PCB. The sensor read-out and data transfer to the PC, through a USB interface, is done by an FPGA-based board developed by the company Arducam (Arducam).

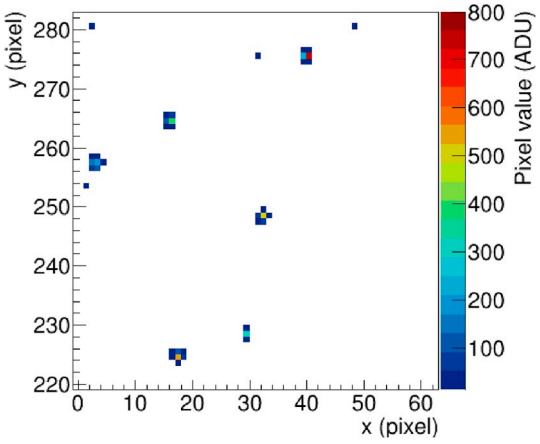

Fig. 3. Example of an image region captured with the CIS. Cluster of pixels that correspond to single X-ray photons interactions can be observed. The white color was assigned to pixels with less than four times the image noise. (For interpretation of the references to color in this figure legend, the reader is referred to the Web version of this article.)

light, a 130 μm thick layer of aluminum was used. The whole system was operated at room temperature without temperature control.

The rolling shutter of the MT9M001 was set in one hundred lines. This makes possible integrate simultaneously one hundred lines of pixels, given a pixel integration time of 6.3 ms (ONSemi). The automatic black level calibration was disabled to avoid adding artifacts to the pixel value.

An X-ray tube with a copper target, model KFF-Cu-4K from Siemens, was used as source. The sensor was not only exposed to the beam photons, the Cu K-lines were also employed to produce fluorescence photons from two samples, thus exposing the sensor to different X-rays lines. The first sample was an iron metal foil, and the second one, a seashell. The current and voltage of the tube and the distance to the sensor were adjusted to have an appropriate X-ray flux to avoid pile-up of events in the image and mainly detect single-photon interaction in the sensor. Fig. 3 is a region of an image captured with the sensor, in which each group of bright pixels is produced by a single interactions of one X-ray.

The pixel offset and gain can be controlled in the MT9M001 CIS. Each group of pixels with same column and row parity have a common variable to control the offset and another variable for the gain. The gain of all the pixels was set at its maximum value of ×15. The offset was adjusted to sample the full pixel noise distribution. Fig. 4a shows a plot of the single-pixel distribution of a dark frame (without X-rays). A group of pixel is centered around ~ 55 ADU and the other around ~ 90 ADU. To remove the bias of each pixel (in order to apply a common threshold during the extraction of X-ray events), the mean of the previous fifteen acquisition of the pixel was subtracted. The resulting pixel distribution is shown in Fig. 4b. It is Gaussian distribution with zero mean and a standard deviation $\sigma \sim 3.11$ ADU. This deviation depends on the electronic read-out noise and thermal generation of carriers, in the following, we will refer to this value as image noise.

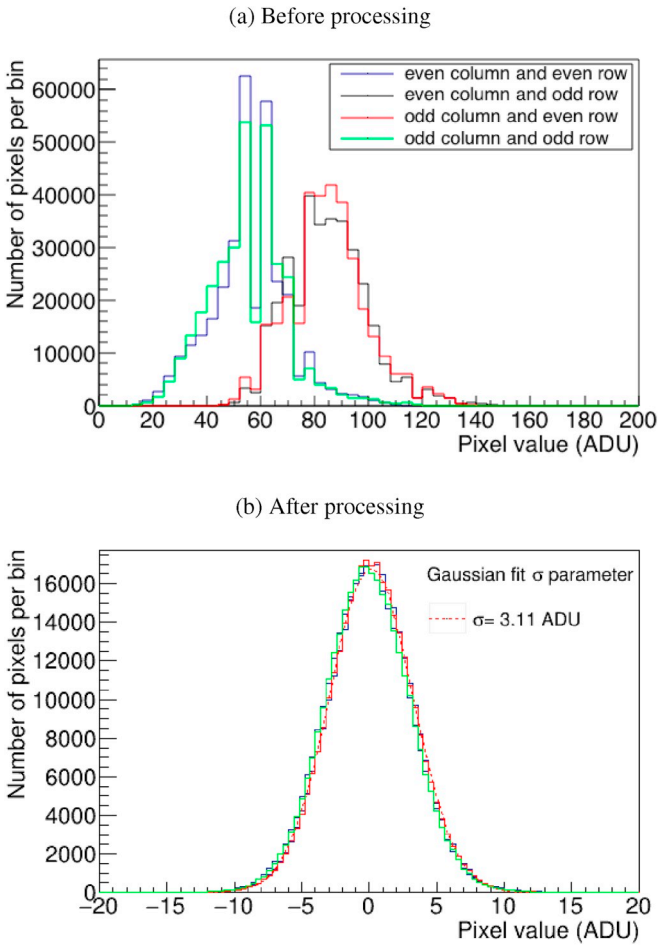

Fig. 4. Single pixel distribution of a dark frame before (4a) and after processing (4b). A Gaussian fit of the distribution of pixel in odd columns and even rows is included, it have a σ of 3.11 ADU, we will refer to this value as image noise.

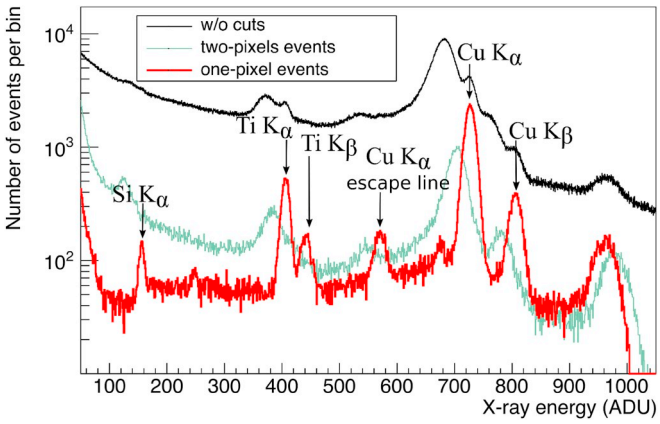

Fig. 5. Spectra obtained by different processing methods, exposing the CIS directly to the X-rays from the tube.

4. Measurement of the X-ray spectrum

To extract the cluster of pixel that correspond to an X-ray interaction, we applied the same method used in CCD particle detection experiments (Chavarria et al., 2015). First, seeds of single or neighboring pixels that have a value more than four times the image noise, this is 4 σ, are identified in the acquired frame. Then, all the pixels around the event seed with more than 3σ are added to form a cluster of pixels that compose the event. The charge of the event is obtained adding all the values of its pixels.

The energy spectrum measured with the CIS exposed to the copper X-rays tube, and to the fluorescence from the metal foil and the seashell, are shown in Figs. 5–7 respectively. The spectrum in black is obtained using all the extracted events. As was formerly exposed in section 2, unless the event occurs in the depleted region of the collection diodes, there will be charge losses due to recombination. This can be observed comparing the spectrums of events with two and one pixels of Fig. 5. For the Cu K_α line, the peak produced by events with signal at two

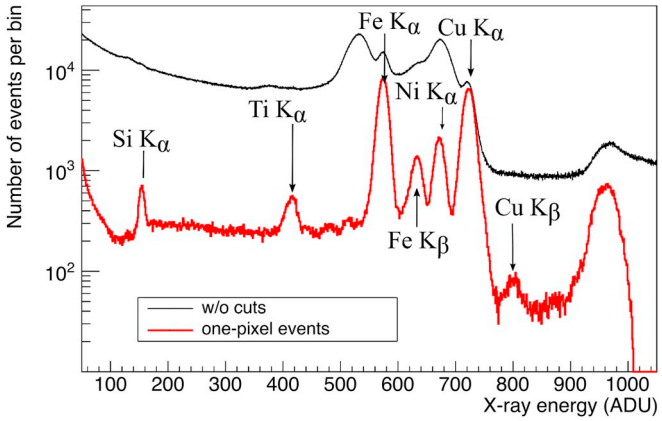

Fig. 6. X-ray spectrum obtained from the fluorescence of a metal foil. The iron K_α and K_β lines can be resolved, as well as the K_α line from nickel.

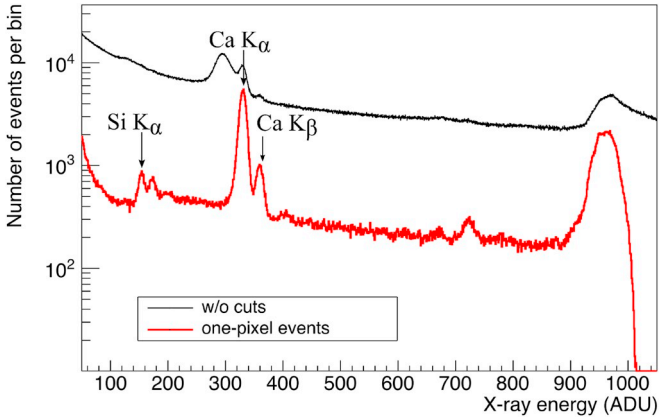

Fig. 7. X-ray spectrum obtained from the fluorescence of a seashell. The calcium K_α and K_β lines are resolved.

pixels is shifted to the right and wider with respect to that due to events with signal in only one pixel. Therefore, the measured charge of events with several pixel underestimates the intensity due to the incomplete charge collection (ICC) formerly described. For this reason, to improve the spectral resolution, an additional cut over the events of only one pixel was implemented. Single pixel events, that have at least in one of the eight closest neighboring pixels, a value more than one sigma of the image noise, were discarded. As shown in the Figs. 5–7, a better resolution is obtained rejecting events with more than one pixel, thus allowing to resolve several X-ray lines.

The spectrum of Fig. 5 shows that the K_α and K_β lines from copper can be resolved, as well as the K_α and K_β lines from the fluorescence of Titanium present in the stainless steel of the X-ray tube. The copper K_α escape line corresponds to an interaction in which a fraction of the energy was firstly deposited and then, as was explained in Section 2, a subsequent silicon K_α photon is emitted that could interact in another pixel and produce the line that is seen in the spectrum.

The counts observed at about ~ 950 ADU in Figs. 5–7, are produced by events that saturate the ADC. The particular shape is introduced by the pixel bias subtraction method, see Fig. 4.

A Gaussian distribution was used to fit each one of the peak. The fits of the peaks from the fluorescence of copper, iron, silicon and calcium are shown in Figs. 8 and 9, 10 and 11 respectively. For the case of iron, a background subtraction was applied. The background was estimated from the direct exposure of the CIS to the X-ray tube (spectrum of Fig. 5). The resulting spectrum is shown in Fig. 9.

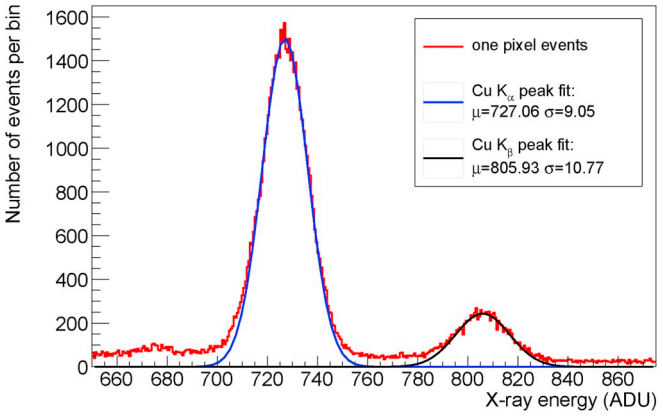

Fig. 8. Fit of fluorescence peaks from copper.

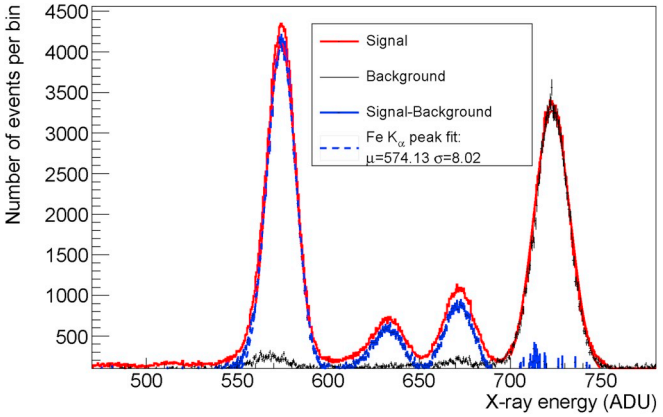

Fig. 9. Fit of the K_α fluorescence peak from the iron of the metal foil.

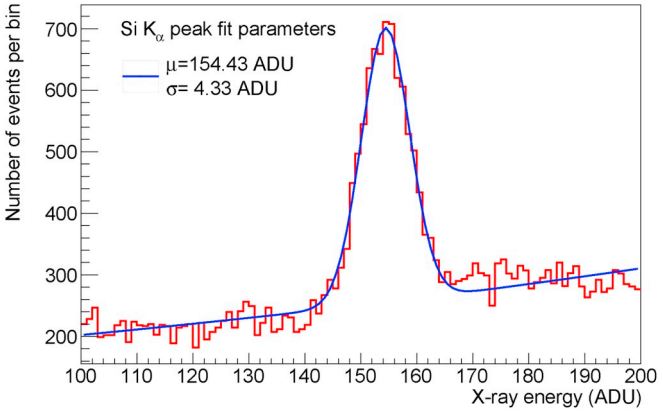

Fig. 10. Fit of the K_α peak from silicon fluorescence. A Gaussian distribution for the peak shape over an exponential background, was fitted to obtain the peak parameters.

5. Results

5.1. Gain and noise

Correlating the energy of the X-ray and the obtained μ parameter, a calibration factor of 90.3 ADU/keV was obtained. The resulting fit is shown in Fig. 12, where a high linearity in the measurement of the X-ray energy is observed.

Taking in account that ~3.64 eV are required in average to generate an electron-hole pair in silicon, the 90.3 ADU/keV conversion gain imply that each ADU corresponds to 3.04 electrons in our configuration

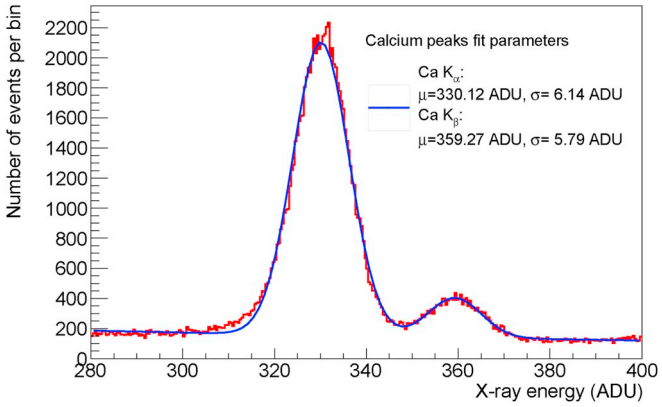

Fig. 11. Fit of K_α and K_β peak from calcium fluorescence. The sum of two Gaussian distribution plus an exponential background was fitted with the spectrum data to extract the peaks parameters.

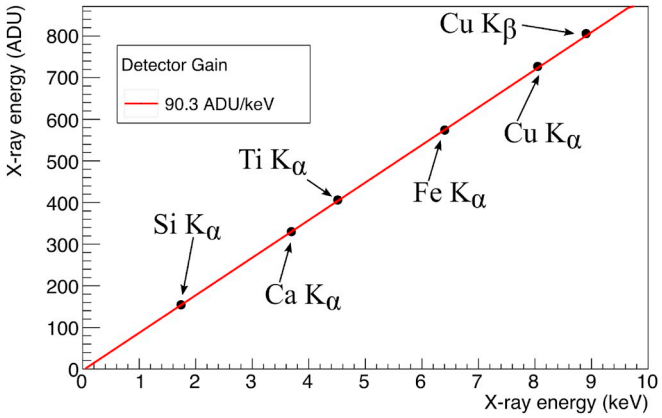

Fig. 12. CIS calibration curve. The CIS shows a linear response in the X-ray energy range measured. The experimental uncertainties of the results are smaller than the symbol size.

with an analog gain of × 15. Considering the pixel saturation of 1.2 V, this implies a conversion gain of the sensor of 22.5 μV/e$^-$, which differs only with the nominal conversion gain of 32 μV/e$^-$ reported by the manufacturer(ONSemi) in a 30% consistent with fabrication process variations in typical submicron CMOS technologies.

Using the previous calibration factor an image noise of 34.4 eV (~ 9.4 e$^-$) was obtained. It corresponds to the standard deviation of the distribution of Fig. 4b, which is consistent with the value reported by the manufacturer of lower than 10 e$^-$ (ONSemi). In a CIS the electronics associated to each pixel is different and therefore will also have different read-out noise. This was analyzed taking 1000 dark frames and calculating the standard deviation of the distribution of the values for each pixel. The result is shown in Fig. 13, the 90% of the pixels have less than ~ 10 e^- of noise.

5.2. Resolution

Table (1) is a summary of the resolution measured of each peak with the MT9M001 CIS. They were obtained multiplying the σ parameter of the Gaussian fit of each peak by the calibration factor of 90.3 ADU/keV.

Fig. 14 shows the resolution obtained from the peak with experimentally observed, as well as the Fano, and the electronic readout contribution. As was expected, ICC deteriorate the spectroscopic resolution, and it is mostly degradated at higher energies. For the peak produced by the Si K_α line, the range of the emitted photo-electron is 0.04 μm, significantly smaller than the device sensitive thickness (~ 2 μm). For this energy, events whit charge losses are less probable

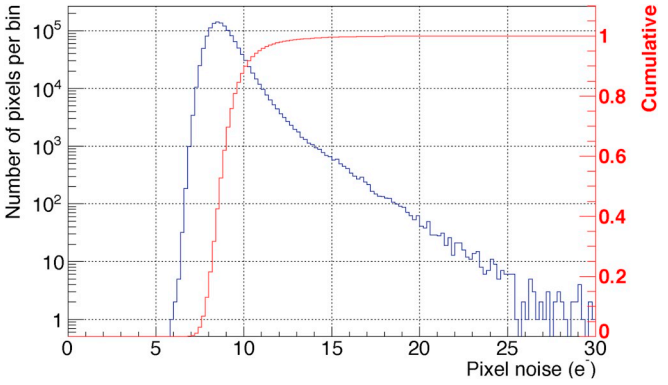

Fig. 13. Distribution of the pixels noise. The 90% of the pixels have less than ~ 10$e^-$of noise.

Table 1
Measured resolution of each X-ray line.

Peak	Energy (keV)	Σ (eV)
Cu K_β	8.90	118.1 ± 3.8
Cu K_α	8.04	99.3 ± 1.5
Fe K_α	6.40	88.0 ± 0.3
Ti K_α	4.51	74.4 ± 1.0
Ca K_α	3.70	67.3 ± 0.27
Si K_α	1.74	47.5 ± 1.2

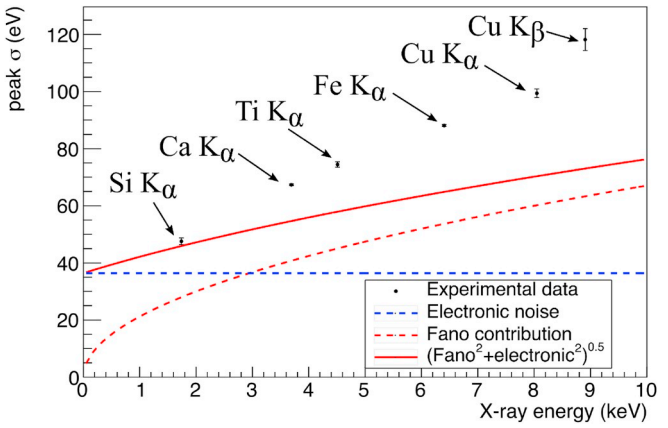

Fig. 14. Peak resolution measured with the MT9M001. A Fano factor of 0.1254 measured at room temperature was used (Perotti and Fiorini, 1999).

that at higher energies, and therefore the resolution is mostly dominated by the read-out noise and Fano contribution.

5.3. Dynamic range

Considering the event extraction method developed in this work, that basically consist on extract only single-pixel events with value more than four times the image noise of 33.5 eV, the minimum observable energy is approximately 136 eV. Taking into account the operation conditions of the MT9M001 described in Section 3, that require a maximum gain as well as to sample the mean value of each pixel, and the dynamic range of the ADC of 1024 ADU, the maximum observable energy is less than 10 keV.

5.4. Quantum efficiency

Although the achieved energy resolution with the CIS is promising and allows to resolve different energy peaks, a low intrinsic quantum efficiency is expected. The MT9M001 micro-lenses and the metal layers

that connect the different chip components produce an attenuation of the incoming X-rays (Bessia et al., 2018). Furthermore, a significant reduction in efficiency is due to the poor depletion volume, which has been estimated to be 14 μm^3 for the MT9M001 (Bessia et al., 2018), that correspond a sensitive thickness of ~1.9 μm.

5.5. Comparison with a SDD

In this work a FWHM of 231.8 eV at 6.4 keV was achieved with the MT9M001 CIS. For example, the well established AMPTEK XR-100 Silicon Drift Detector (SDD) (AMPTEK, 2019) used in X-ray spectroscopy, which operates 85° below ambient temperature has a FWHM of 122 eV at 5.9 keV and a read-out noise of 4.5 e^-; only a half of the value reported in this paper for an uncooled, low cost device which can be easily integrated in an embedded system. The disadvantage of the commercial CIS are the smaller sensitive thickness of 1–2 μm (Meroli et al., 2012) (Bessia et al., 2018), thinner than the attenuation length of the X-ray photons, which reduces the detection efficiency compared to the 500 μm thick SSD. However, the pixelated nature of the CIS, combined with the ability of measuring photon energy demonstrated in this work allows potential applications in energy sensitive X-ray imaging where an SDD cannot be used.

6. Conclusions

We have demonstrated the capability of a commercial and low cost CIS to resolve several X-rays peaks in the range from ~ 1.7–9 keV, without cooling the detector. For first time the energy resolution of this devices was measured and analyzed for soft X-rays. The contribution of the read-out noise, Fano noise and ICC, to the resolution was studied, being the ICC the dominant factor at higher energies. A resolution comparable to a professional SDD was obtained. CIS are therefore a valid option as low cost and easy access X-ray detector, for example, for educational purposes. Besides, the possibility of combining high resolution X-ray imaging and spectroscopy in a single-device could allow CIS to be used as the replacements of more expensive detection technologies in several biological and material sciences applications.

Acknowledgment

The authors would like to thank to Ignacio Artola for his help with the experimental setup, to Jorge Pelegrina for the use of X-ray sources, and to Sergio Suarez for provide the samples.This work was supported by the ANPCyT under Project PICT-2014-1966, Project PICT-2015-1644 and Project PICT-2015-2128, by UNCuyo under Grant C018, and in part by CONICET under Project PIP-2011-0552 and Project PIP-2013-0077.

References

Alcalde Bessia, F., Pérez, M., Lipovetzky, J., Piunno, N.A., Mateos, H., Sidelnik, I., Blostein, J.J., Sofo Haro, M., Gómez Berisso, M., 2018. X-ray micrographic imaging system based on cots cmos sensors. Int. J. Circuit Theory Appl. 46 (10), 1848–1857.

AMPTEK. http://amptek.com/products/xr-100sdd-silicon-drift-detector. Accessed: 2019-05-04.

Arducam. http://www.arducam.com/arducam-usb-camera-shield-released/. Accessed: 2018-12-5.

Ashley, J., Tung, C., Ritchie, R., Anderson, V., 1976. Calculations of mean free paths and stopping powers of low energy electrons (¡10 kev) in solids using a statistical model. IEEE Trans. Nucl. Sci. 23 (6), 1833–1837.

Bessia, F.A., Pérez, M., Haro, M.S., Sidelnik, I., Blostein, J.J., Suárez, S., Pérez, P., Berisso, M.G., Lipovetzky, J., 2018. Displacement damage in cmos image sensors after thermal neutron irradiation. IEEE Trans. Nucl. Sci. 65 (11), 2793–2801.

Castoldi, A., Guazzoni, C., Maffessanti, S., Montemurro, G.V., Carraresi, L., 2015. Commercial cmos image sensors as x-ray imagers and particle beam monitors. J. Instrum. 10 (01), C01002.

Chavarria, A.E., Tiffenberg, J., Aguilar-Arevalo, A., Amidei, D., Bertou, X., Cancelo, G., D'Olivo, J.C., Estrada, J., Moroni, G.F., Izraelevitch, F., et al., 2015. Damic at snolab. Physics Procedia 61, 21–33.

Esposito, M., Price, T., Anaxagoras, T., Allinson, N., 2017. Geant4-based simulations of charge collection in cmos active pixel sensors. J. Instrum. 12 (03), P03028.

Groom, D., et al., 2004. Temperature Dependence of Mean Number of Eh Pairs Per Ev of X-Ray Energy Deposit. wwwccd_lbl_gov/w Si_pdf.

Grupen, C., Shwartz, B., 2008. Particle Detectors, vol. 26 Cambridge university press.

Hoidn, O.R., Seidler, G.T., 2015. Note: A disposable x-ray camera based on mass produced complementary metal-oxide-semiconductor sensors and single-board computers. Rev. Sci. Instrum. 86 (8) 086107.

Holden, W.M., Hoidn, O.R., Seidler, G.T., DiChiara, A.D., 2018. A color x-ray camera for 2–6 kev using a mass produced back illuminated complementary metal oxide semiconductor sensor. Rev. Sci. Instrum. 89 (9) 093111.

Janesick, J., 2001. Scientific Charge-Coupled Devices. Press Monographs. Society of Photo Optical.

Lane, D.W., 2012. X-ray imaging and spectroscopy using low cost cots cmos sensors. Nucl. Instrum. Methods Phys. Res. Sect. B Beam Interact. Mater. Atoms 284, 29–32.

Meroli, S., Biagetti, D., Passeri, D., Placidi, P., Servoli, L., Tucceri, P., 2011. A grazing angle technique to measure the charge collection efficiency for cmos active pixel sensors. Nucl. Instrum. Methods Phys. Res. Sect. A Accel. Spectrom. Detect. Assoc. Equip. 650 (1), 230–234.

Meroli, S., Passeri, D., Servoli, L., 2012. Measurement of charge collection efficiency profiles of cmos active pixel sensors. J. Instrum. 7 (09), P09011.

Moody, I., Watkins, M., Bell, R., Soman, M., Keelan, J., Holland, A., 2017. Ccd qe in the Soft X-Ray Range.

Nachtrab, F., Hofmann, T., Firsching, M., Uhlmann, N., Hanke, R., 2009. Simple solutions for spectroscopic, photon counting x-ray imaging detectors. In: Nuclear Science Symposium Conference Record (NSS/MIC), 2009 IEEE. IEEE, pp. 1636–1639.

ON Semiconductor. https://www.onsemi.com/. Accessed: 2019-04-20.

Perotti, F., Fiorini, C., 1999. Observed energy dependence of Fano factor in silicon at hard X-ray energies. Nucl. Instrum. Methods Phys. Res. Sect. A Accel. Spectrom. Detect. Assoc. Equip. 423 (2–3), 356–363.

Prigozhin, G., Jones, S., Bautz, M., Ricker, G., Kraft, S., 2000. The physics of the low-energy tail in the ACIS CCD: The spectral redistribution function. Nucl. Instrum. Methods Phys. Res. Sect. A Accel. Spectrom. Detect. Assoc. Equip. 439 (2–3), 582–591.

Schroder, D.K., 1997. Carrier lifetimes in silicon. IEEE Trans. Electron Devices 44 (1), 160–170.

Watson, E.C., 1928. The space-distribution of the photo-electrons ejected by X-rays. Phys. Rev. 31 (5), 728.

Williams, G.P., 2001. X-ray Data Booklet. X-ray data booklet.

Yousef, H., 2011. Energy Dependent Charge Spread Function in a Dedicated Synchrotron Beam pnCCD Detector. Universität Siegen, Siegen, Germany Ph.D. thesis; Ph. D thesis.

Further reading

Fraser, G., Abbey, A., Holland, A., McCarthy, K., Owens, A., Wells, A., 1994. The x-ray energy response of silicon part a. theory. Nucl. Instrum. Methods Phys. Res. Sect. A Accel. Spectrom. Detect. Assoc. Equip. 350 (1–2), 368–378.

ORTEC, E., 1994. Modular Pulse-Processing Electronics and Semiconductor Radiation Detectors. EG&G Ortec, Tenesse, USA.